

FOR REFERENCE

NOT TO BE TAKEN FROM DESK

Numerical Study of Porous Airfoils in Transonic Flow

Chung-Lung Chen, Chen-Yen Chow, Terry L. Holst
and William R. Van Dalsem

May 1985

LIBRARY COPY

JUL 24 1985

LANGLEY RESEARCH CENTER
LIBRARY, NASA
HAMPTON, VIRGINIA



National Aeronautics and
Space Administration



NF00001

Numerical Study of Porous Airfoils in Transonic Flow

Chung-Lung Chen and Chen-Yen Chow, University of Colorado, Boulder, Colorado
Terry L. Holst and William R. Van Dalsem, Ames Research Center, Moffett Field,
California

May 1985



National Aeronautics and
Space Administration

Ames Research Center
Moffett Field, California 94035

1188-27808-1

NUMERICAL STUDY OF POROUS AIRFOILS IN TRANSONIC FLOW

Chung-Lung Chen,¹ Chuen-Yen Chow,¹ Terry L. Holst, and William R. Van Dalsem

Ames Research Center

SUMMARY

A numerical study was made to examine the effect of a porous surface on the aerodynamic performance of a transonic airfoil. The pressure jump across the normal shock wave on the upper surface of the airfoil was reduced by making the surface below the shock porous. The weakened shock is preceded by an oblique shock at the upstream end of the porous surface where air is blown out of the cavity. The lambda shock structure shown in the numerical result qualitatively agrees with that observed in the wind tunnel. According to the present analysis, the porous airfoil has a smaller drag and a higher lift than the solid airfoil.

INTRODUCTION

The transonic flow past an airfoil in flight at a high subsonic Mach number is characterized by a normal shock wave standing on the upper surface. If the airfoil surface in the neighborhood of the shock wave is made porous with a cavity underneath it (as sketched in fig. 1), the pressure difference across the shock induces a flow through the cavity. The passive blowing and suction through the upper surface, before and after the shock respectively, reduces the strength of the shock. It can be expected that the wave drag of the porous airfoil is decreased.

This expectation has been proven by the experimental results obtained by Bahi et al. and Nagamatsu et al. (refs. 1 and 2) which indicate that at high subsonic Mach numbers a properly arranged porosity can reduce both wave and viscous drag. In these experiments, however, the airfoil model was mounted so that the lower half of the airfoil was embedded in the bottom wall of the test section and only the upper surface was exposed to the transonic flow. This experimental condition is different from free flight. The negligible loss in lift on the porous airfoil reported in references 1 and 2 might not be the appropriate conclusion for a lifting airfoil.

Numerical computations of the flow about a porous NACA 0012 airfoil were performed by Savu and Trifu (ref. 3) by solving the transonic small-perturbation potential equation. Their results, for the airfoil at zero incidence and with the same porosity distribution on both the upper and lower surfaces, show that the standing shock may be eliminated completely by choosing a proper distribution of porosity for

¹University of Colorado, Boulder, Colorado.

a given Mach number. Additional references on thin airfoils with porous surfaces in pure subsonic or pure supersonic regimes can be found in reference 3.

The aforementioned experimental and theoretical results indicate that porous surfaces can be used to reduce the wave drag of an airfoil at transonic speeds. Unlike a supercritical airfoil whose fixed shape is designed for certain optimum Mach number and angle-of-attack ranges, a porous airfoil can be adjusted without changing its contour shape. This adjustment is achieved with variable surface porosity and may result in improved performance over a wide range of conditions.

The aerodynamic performance of a symmetrical airfoil in inviscid transonic flow with a partial porous surface is examined in the present work. Instead of the small-perturbation equation with linearized boundary conditions used in reference 3, the transonic full-potential equation is solved with boundary conditions applied exactly on the airfoil surface. The analysis also includes the influence of angle of attack which was ignored in previous computational studies.

The work of the first two authors was supported by the U.S. Air Force Office of Scientific Research under Grant AFOSR 84-0037. Their use of the office and computing facilities at NASA Ames Research Center is highly appreciated.

ANALYSIS

Because the entropy jump across the shock is third order, inviscid transonic flow is approximated as an isentropic and irrotational flow. This assumption allows the flow to be described by a potential ϕ which satisfies the continuity equation.

$$(\rho\phi_x)_x + (\rho\phi_y)_y = 0 \quad (1a)$$

$$\rho = \left[1 - \frac{\gamma-1}{\gamma+1} (\phi_x^2 + \phi_y^2) \right]^{1/(\gamma-1)} \quad (1b)$$

where x and y are Cartesian coordinates nondimensionalized by the airfoil chord length c ; ρ and ϕ_x, ϕ_y are the density and velocity components nondimensionalized by the stagnation density ρ_s and the critical sound speed a^* , respectively; and γ is the ratio of specific heats. Equation (1a) (the full-potential equation) is written in strong conservation law form which is an important consideration for shock capturing algorithms.

For computational convenience, these equations are transformed from the physical domain (Cartesian coordinates) to a computational domain by the transformation (see fig. 2)

$$\xi = \xi(x,y) \quad \eta = \eta(x,y) \quad (2)$$

The full-potential equation written in the computational domain (ξ - η coordinate system) is given by

$$(\rho U/J)_{\xi} + (\rho V/J)_{\eta} = 0 \quad (3a)$$

$$\rho = \left[1 - \frac{\gamma - 1}{\gamma + 1} (U\phi_{\xi} + V\phi_{\eta}) \right]^{1/(\gamma-1)} \quad (3b)$$

where

$$U = A_1\phi_{\xi} + A_2\phi_{\eta} \quad V = A_2\phi_{\xi} + A_3\phi_{\eta}$$

$$A_1 = \xi_x^2 + \xi_y^2$$

$$A_2 = \xi_x\eta_x + \xi_y\eta_y$$

$$A_3 = \eta_x^2 + \eta_y^2$$

and

$$J = \xi_x\eta_y - \xi_y\eta_x$$

The variables U and V are the contravariant velocity components along the ξ and η directions, respectively; A_1 , A_2 , and A_3 are metric quantities; and J is the Jacobian of the transformation.

The body-fitted grids used in this work are generated by the finite difference solution of Poisson's equations using a computer code (GRAPE) developed by Sorenson (ref. 4) and based on the work of Steger and Sorenson (ref. 5). This grid generation code allows control of both grid point spacing along and normal to the boundaries and the angles at which grid lines intersect the boundaries. The C-mesh grid topology used in this study is shown in figure 2.

The governing equations (eqs. (3)) are solved using a fully implicit approximate factorization scheme called AF2. A modified version of the TAIR computer program is used for this purpose (refs. 6 and 7). This code provides rapid convergence requiring only a few seconds of computer time per case on the CRAY XMP computer. The supersonic regions of flow are stabilized using an upwind bias of the density. This provides an efficient and reliable spatial differencing scheme for the capture of weak (transonic) shock waves. For more information about the flow solver algorithm or the TAIR computer program see references 6 and 7.

The boundaries associated with the physical domain are transformed to boundaries of the computational domain. At the outer boundary, the velocity potential is set as the sum of the uniform free-stream component and the component due to a vortex with circulation Γ , where Γ is the jump in the velocity potential at the airfoil trailing edge. At the airfoil surface, there are two types of boundary conditions depending on the surface property.

1. On solid regions of the airfoil, the flow tangency condition is satisfied by requiring that the contravariant velocity component in the η -direction vanish.

$$V = 0 \quad \text{on solid surface} \quad (4)$$

2. On porous regions of the airfoil, V does not vanish and its value is determined in the following manner. Through the porous surface the transpiration velocity v_n is governed by Darcy's law such that

$$v_n = -(1/2)\sigma(C_p - \bar{C}_p) \quad (5a)$$

$$\sigma = \bar{\sigma}U_\infty/a^* \quad (5b)$$

where the subscript n indicates the direction of the outward normal on the surface; C_p and \bar{C}_p are the pressure coefficients above and below the porous surface, respectively; $\bar{\sigma}$ is the porosity distribution function which is determined by viscosity as well as by the size and density of the holes in the porous surface. For passive flow through the cavity, the net mass flow through the porous surface of length s must be zero, or

$$Q = \int_S \rho v_n \, ds = 0$$

which gives, by assuming a constant cavity pressure,

$$\bar{C}_p = \int_S \sigma \rho C_p \, ds / \int_S \sigma \rho \, ds \quad (6)$$

The constant cavity pressure assumption was made for convenience but is expected to be qualitatively accurate. In addition, several variations of porosity have been investigated with the expectation that this would simulate a variable cavity pressure. It is planned that additional work to improve the cavity flow numerical model will be completed in the near future.

The transpiration velocity v_n computed from equations (5) is then transformed into the computational domain (ref. 8):

$$\begin{bmatrix} V \\ U \end{bmatrix} = \begin{bmatrix} \sqrt{A_3} & 0 \\ A_2/\sqrt{A_3} & J/\sqrt{A_3} \end{bmatrix} \begin{bmatrix} v_n \\ 0 \end{bmatrix} \quad (7a)$$

With the C-mesh topology, the η -coordinate lines intersect the body at close to right angles, and to a good approximation $A_2 \approx 0$ at the body. Using this approximation v_n does not contribute to U and can be expressed in the computational domain as:

$$V = \sqrt{A_3} v_n \quad \text{on the porous surface} \quad (7b)$$

The numerical implementation of the boundary conditions on the airfoil surface is outlined as follows:

1. On the solid portion of the airfoil, the boundary condition of flow tangency (i.e., $V = 0$) is used to obtain

$$\left(\frac{\rho V}{J}\right)_{1,NJ+(1/2)} = -\left(\frac{\rho V}{J}\right)_{1,NJ-(1/2)} \quad (8)$$

where $j = NJ$ is the airfoil surface (see fig. 2).

2. On the porous portion of the airfoil, the boundary condition (i.e., $V = \sqrt{A_3} v_n$) is applied with the aid of Taylor series expansions

$$\left(\frac{\rho V}{J}\right)_{1,NJ\pm(1/2)} = \left(\frac{\rho V}{J}\right)_{1,NJ} \pm \frac{\Delta\eta}{2} \left(\frac{\rho V}{J}\right)'_{1,NJ} + \frac{(\Delta\eta)^2}{8} \left(\frac{\rho V}{J}\right)''_{1,NJ} \pm O[(\Delta\eta)^3] \dots \quad (9)$$

so that the first-order boundary condition becomes

$$\left(\frac{\rho V}{J}\right)_{1,NJ+(1/2)} = -\left(\frac{\rho V}{J}\right)_{1,NJ-(1/2)} + 2 \left(\frac{\rho V}{J}\right)_{1,NJ} \quad (10)$$

In fact, equation (8) is a special case of equation (10) for $V = 0$ at $j = NJ$. For more information on the transpiration velocity boundary condition see reference 8.

Equations (3), together with the surface boundary conditions (eqs. (8) and (10)) and appropriate outer boundary conditions, are solved numerically using the modified TAIR computer code. At the beginning of each iteration, the porous boundary condition is updated using equations (5).

Once the flow field is obtained, forces on the airfoil in the x and y directions can be computed by performing integrations around the airfoil contour.

$$F_x = \int_S (pn_x + \rho v_n u) ds \quad (11)$$

$$F_y = \int_S (pn_y + \rho v_n v) ds \quad (12)$$

in which S is the circumference of the airfoil; u and v are velocity components in the x and y directions, respectively; and n_x and n_y are direction cosines between the airfoil surface and the x and y directions, respectively. Equations (11) and (12) are derived from the momentum conservation theorem. Note that the second term in both equations ($\rho v_n u$ and $\rho v_n v$) are zero for solid wall airfoils but must be retained in the present calculations because of the porous wall assumption. Once F_x and F_y are obtained from equations (11) and (12), the lift and drag coefficients, C_L and C_D , are easily computed.

NUMERICAL EXPERIMENTS AND RESULTS

A NACA 0012 airfoil was used for a series of numerical studies to investigate the effect of a porous surface on its transonic flight performance. In all of the cases presented here, computations were carried out on a 223×31 C-type mesh, having 162 of the 6913 grid points placed on the airfoil surface.

Three types of porosity distribution have been examined which were obtained by varying the porosity distribution function $\bar{\sigma}$ in equation (5b). They are described as follows:

Type 1

$$\bar{\sigma} = \text{constant} \quad (13)$$

Type 2

$$\bar{\sigma} = \bar{\sigma}_{\max} \sqrt{\sin \frac{x - x_1}{x_2 - x_1} \pi} \quad (14)$$

the x_1 and x_2 parameters are the limits of the porous region shown in figure 1, and $\bar{\sigma}_{\max}$ is the maximum porosity at the midpoint of that region. The Type 2 porosity distribution is the same distribution function used by Savu and Trifu (ref. 3).

Type 3

$$\bar{\sigma} = \bar{\sigma}_{\max} \sqrt{\cos \frac{x - x_s}{x_k - x_s} \frac{\pi}{2}} \quad (15)$$

The x_s parameter is the horizontal position of the shock that would result if the porous surface were solid, and x_k represents either x_1 or x_2 , depending on whether x is less or greater than x_s . This function automatically adjusts the porosity distribution so that it decreases from the maximum value $\bar{\sigma}_{\max}$ under the shock wave to zero at either end of the porous region. Numerical experiments indicate that, in most cases, the Type 2 and 3 distribution functions are superior to the uniform $\bar{\sigma}$ distribution for drag reduction. For this reason, the results obtained based on the Type 1 distribution function are not reported here.

The effect of a porous surface on a Mach 0.8 flow past the NACA 0012 airfoil at zero angle of attack is presented in figures 3 and 4. A Type 2 porosity is distributed on the upper surface between $x_1 = 0.4$ and $x_2 = 0.8$ with $\bar{\sigma}_{\max} = 0.6$. The constant-Mach number contours show a normal shock standing below the solid lower surface of the porous airfoil whose location and strength are not much different from those of the shock on the original solid airfoil. However, the shock above the upper surface is weakened in the presence of the porous surface, as shown by a group of less concentrated constant-Mach lines around the sonic line. The figure also reveals that the porous surface causes a weak oblique compression wave at its upstream end ($x_1 = 0.4$), due to the blowing from the cavity, and a readjusted compression downstream of the shock due to the suction of air into the cavity. The contour lines in the shock region are no longer normal to the airfoil surface, resulting in a lambda-shaped shock wave structure similar to that photographed in the laboratory (refs. 1 and 2).

The pressure distribution on the upper airfoil surface for the case just presented is plotted in figure 4. The results for both a porous airfoil (dashed line) and solid airfoil (solid line) are compared. The comparison clearly shows that the original steep compression through the normal shock on the solid airfoil has been reduced in the presence of the porous region. The original shock is replaced by several weaker compressions over the region covered by the porous surface. The resulting weaker adverse pressure gradient would lessen the possibility of flow separation. The porous upper surface has a negligible influence on the pressure distribution along the lower surface; that distribution is, therefore, omitted here. The asymmetrical pressure distribution on the upper and lower surfaces causes a small lift on the airfoil at zero angle of attack, with $C_L = 0.0183$. On the other hand, a 27.5% decrease in wave drag from $C_D = 0.0069$ to 0.0050 is found for the porous airfoil.

Much larger decreases in drag are obtained when both upper and lower surfaces are made porous. The effect of varying the porosity strength on the drag of a double-porous NACA 0012 airfoil at $\alpha = 0^\circ$ is shown in figure 5. A Type 2 porosity distribution between $x_1 = 0.1$ and $x_2 = 1.0$ is used for all curves presented. The porous surface has a drag-reduction effect only when a shock appears above it at

Mach numbers higher than 0.77, and that effect is enhanced by increasing $\bar{\sigma}_{\max}$ (i.e., by using porous surfaces having smaller resistance to the penetrating flow).

With the same $\bar{\sigma}_{\max}$, changing from Type 2 to Type 3 porosity does not cause a significant change in drag if the normal shock appears near the center of the porous surface; otherwise Type 3 porosity is considerably better than Type 2 in smearing the shock and reducing the drag.

It is not possible to make a direct comparison of the computed data shown in figure 5 with the experimental results presented in reference 2 obtained in the wind tunnel under a different flow arrangement. Furthermore, the measured drag data contain the effects of viscosity, airfoil surface roughness, and other factors that have not been considered in our analysis. Nevertheless, the drag reduction effect caused by the porous surface observed in the laboratory is qualitatively the same as that obtained in the present study.

The behavior of porous airfoils at angle of attack is now described. The Mach number contours for a solid NACA 0012 airfoil at Mach 0.75 and an angle of attack of 1° are plotted in figure 6. A shock wave appears only on the upper surface. A Type 3 porosity of strength $\bar{\sigma}_{\max} = 0.3$ is then distributed on 90% of the upper surface between $x_1 = 0.1$ and $x_2 = 1.0$. The resulting flow pattern and pressure distribution, plotted in figures 7 and 8, respectively, reveal that this widely distributed porosity is very effective in reducing the shock strength. By making the upper surface porous, C_L increases from 0.2397 to 0.3566 while C_D decreases from 0.0024 to 0.0008, which corresponds to a nearly shock-free condition.

To study the effect of varying porosity strength on lift and drag of a transonic airfoil, a Type 3 porosity is distributed between $x_1 = 0.3$ and $x_2 = 0.9$ on the upper surface of a NACA 0012 airfoil. For this series of cases the angle of attack is fixed at 1° . The result for drag plotted in figure 9 is analogous to that shown in figure 5 for the double-porous airfoil at zero angle of attack, showing that large drag reductions can be achieved by increasing the porosity. Plotted in figure 10 are the lift coefficient data which indicate that lift is increased by making the upper surface porous. Unlike the drag coefficient, C_L is affected by the porous surface at Mach numbers less than 0.72 when the shock is still upstream of the porous region. The higher lift is caused by asymmetric changes in the pressure on the porous upper and solid lower surfaces of the airfoil.

CONCLUDING REMARKS

The numerical solution to the full-potential equation shows that the drag of a transonic airfoil can be reduced when a porous surface is placed in the shock region, and that the drag reduction ability increases with increasing porosity $\bar{\sigma}_{\max}$. For an airfoil having porous upper and lower surfaces at zero incidence, the results reported in reference 3 agree qualitatively with those obtained here without using the small-disturbance approximation. Computed flow fields display the lambda shock structure that has been observed in the laboratory. It is also found that the

porous upper surface alone causes not only a reduced drag, but also an increased lift on a transonic airfoil at angle of attack.

The outcome of our preliminary study of using a porous surface for drag reduction is encouraging. In our continued study we will refine the present potential flow model by computing the internal cavity flow instead of assuming that the cavity pressure is constant. Thus the shape of the cavity will have an influence on the drag, which is a fact already being found experimentally (ref. 1). Viscous and three-dimensional effects will also be implemented to simulate the flow more realistically. Finally, this work will be extended to handle both passive and forced suction and blowing on the airfoil surface.

REFERENCES

1. Bahi, L.; Ross, J. M.; and Nagamatsu, H. T.: Passive Shock Wave/Boundary Layer Control for Transonic Airfoil Drag Reduction. AIAA Paper 83-0137, Jan. 1983.
2. Nagamatsu, H. T.; Orozco, R. D.; and Ling, D. C.: Porosity Effect on Supercritical Airfoil Drag Reduction by Shock Wave/Boundary Layer Control. AIAA Paper 84-1682, June 1984.
3. Savu, G.; and Trifu, O.: Porous Airfoils in Transonic Flow. AIAA Journal, vol. 22, July 1984, pp. 989-991.
4. Sorenson, R. L.: A Computer Program to Generate Two-Dimensional Grids About Airfoils and Other Shapes by the Use of Poisson's Equation. NASA TM-81198, May 1980.
5. Steger, J. L.; and Sorenson, R. L.: Automatic Mesh-Point Clustering Near a Boundary in Grid Generation with Elliptic Partial Differential Equations. Journal of Computational Physics, vol. 33, Dec. 1979, pp. 405-410.
6. Holst, T. L.: Implicit Algorithm for the Conservative Transonic Full-Potential Equation Using an Arbitrary Mesh. AIAA Journal, vol. 17, Oct. 1979, pp. 1038-1045.
7. Dougherty, F. C.; Holst, T. L.; Gundy, K. L.; and Thomas, S. D.: TAIR-A Transonic Airfoil Analysis Computer Code. NASA TM-81296, May 1981.
8. Van Dalsem, W. R.: Simulation of Separated Transonic Airfoil Flow by Finite-Difference Viscous-Inviscid Interaction. Ph.D. dissertation, Stanford University, June 1984.

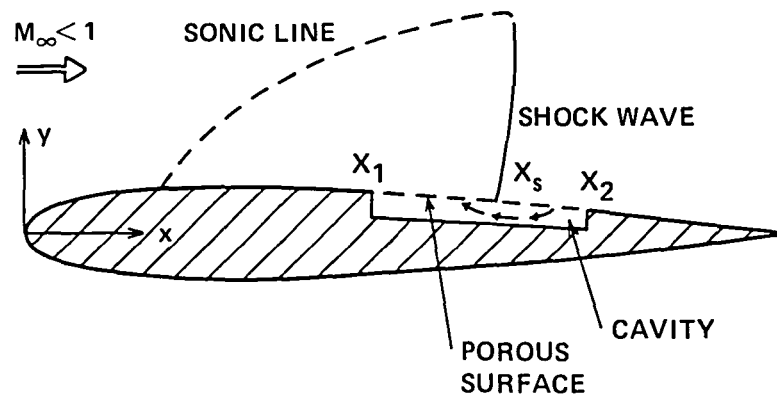
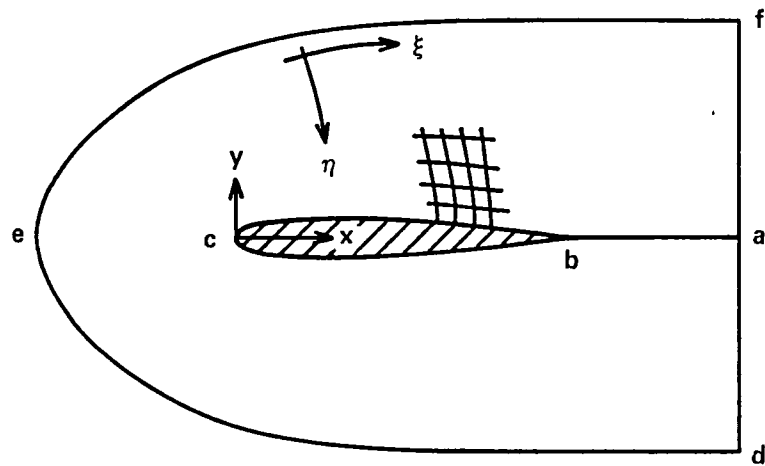
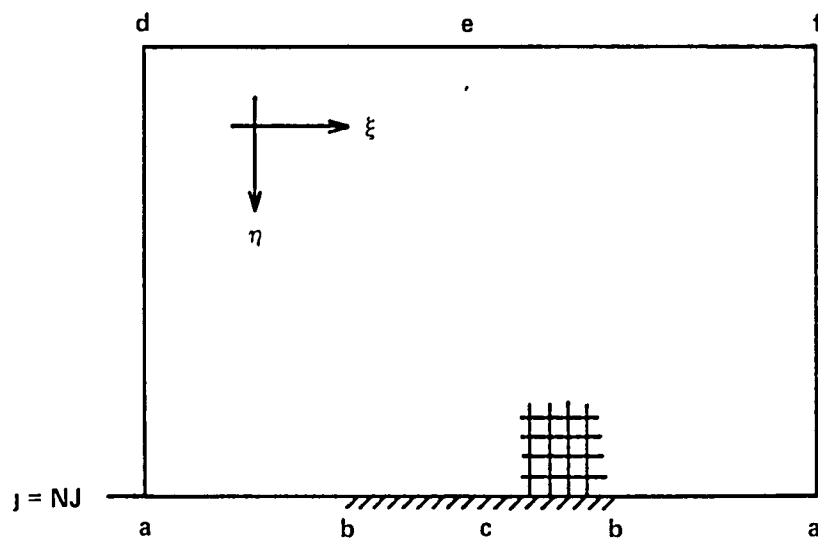


Figure 1.- Porous airfoil in transonic flow.

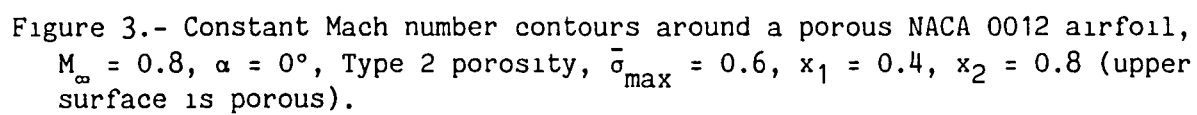


(a) Physical domain.



(b) Computational domain.

Figure 2.- C-grid topology for numerical computation.



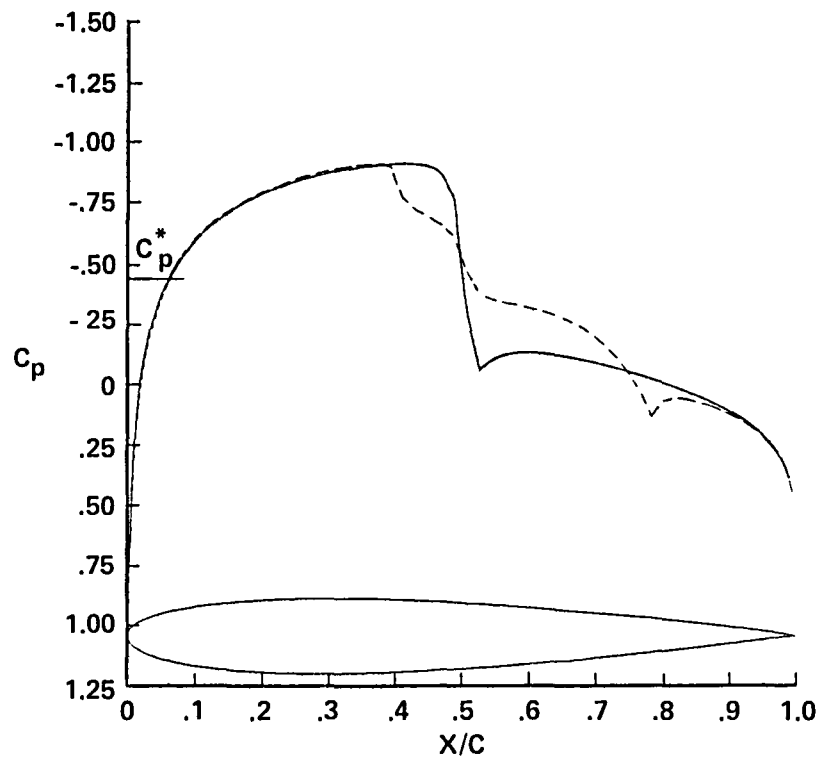


Figure 4.- Pressure distribution on the upper surface of the airfoil described in figure 3, porous airfoil--dashed line, solid airfoil--solid line.

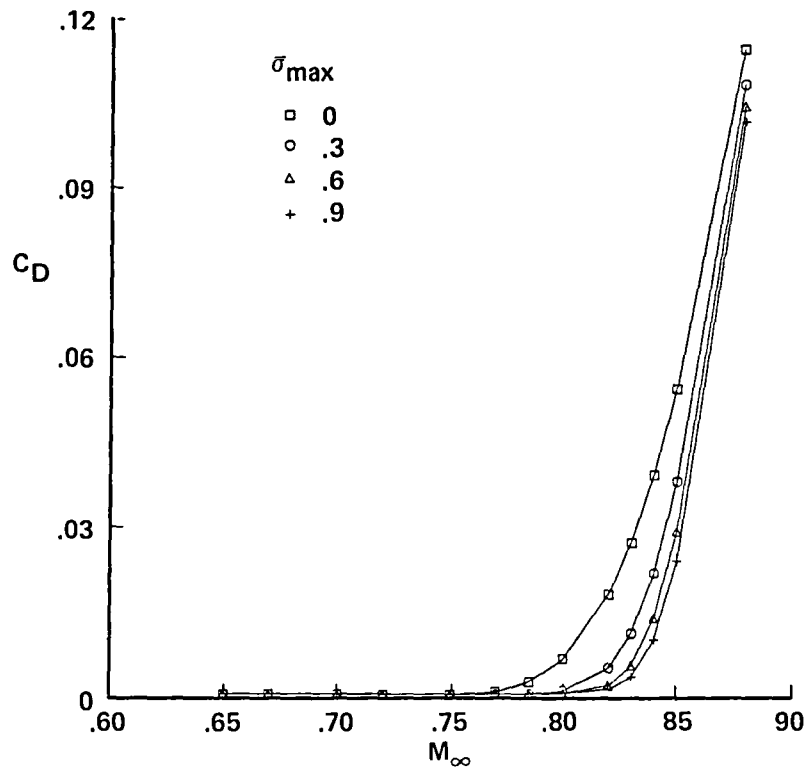


Figure 5.- Effect of varying porosity strength on the drag of a NACA 0012 airfoil at $\alpha = 0^\circ$, Type 2 porosity, $x_1 = 0.1$, $x_2 = 1.0$ (both the upper and lower surfaces are porous).

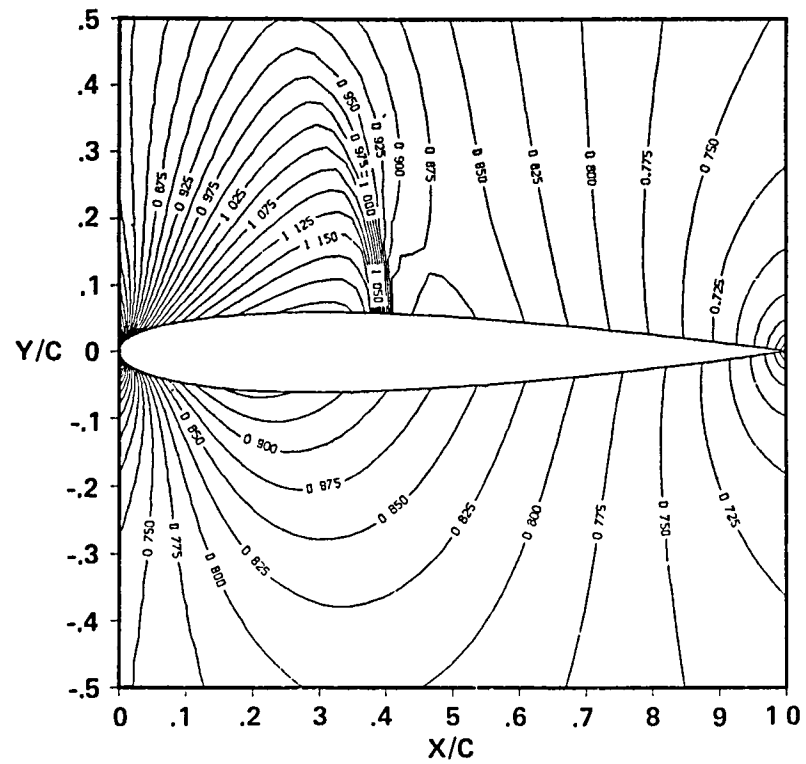


Figure 6.- Constant Mach number contours around a solid NACA 0012 airfoil for $M_{\infty} = 0.75$ and $\alpha = 1^\circ$.

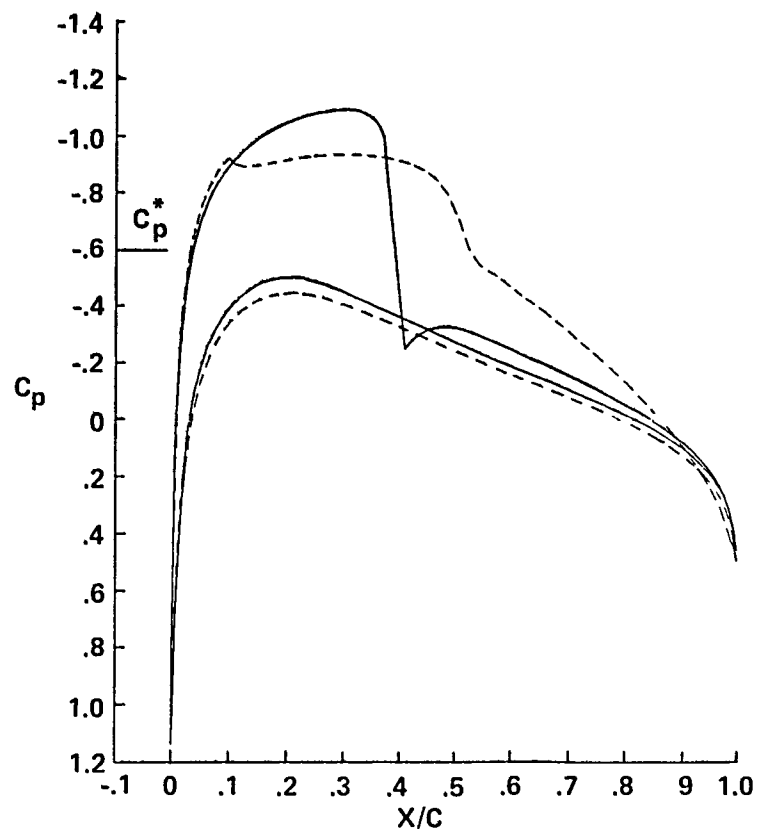


Figure 8.- Pressure distribution around the airfoil described in figure 7, porous airfoil--dashed line, solid airfoil--solid line.

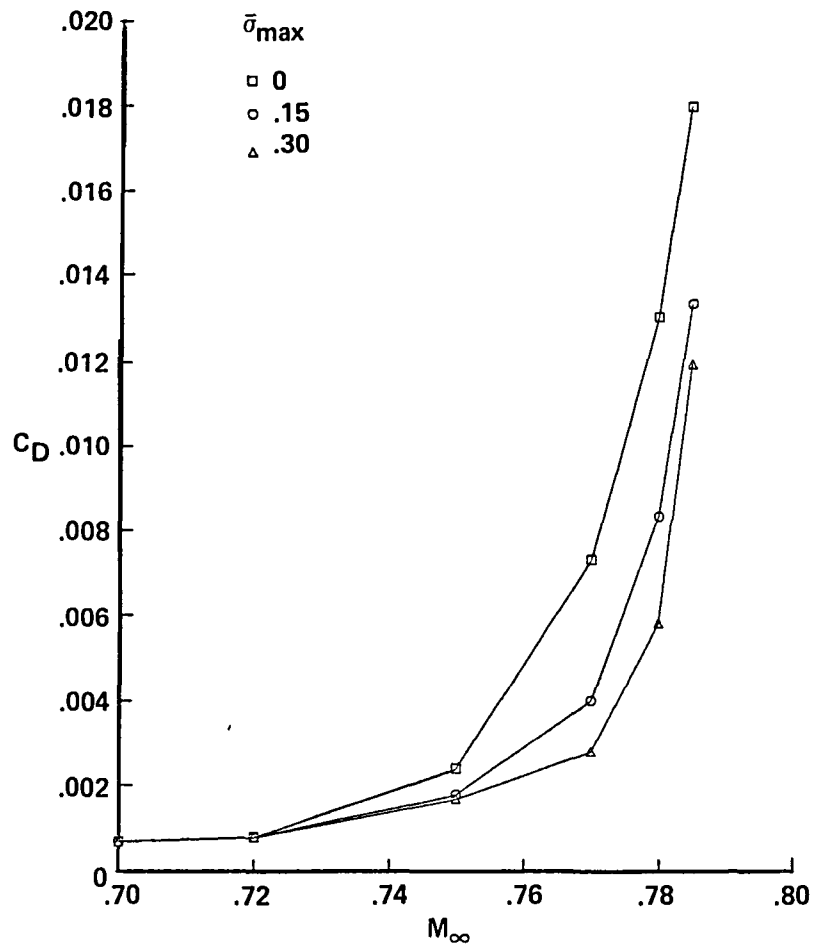


Figure 9.- Effect of varying porosity strength on the drag of a NACA 0012 airfoil at $\alpha = 1^\circ$, Type 3 porosity, $x_1 = 0.3$, $x_2 = 0.9$ (upper surface is porous).

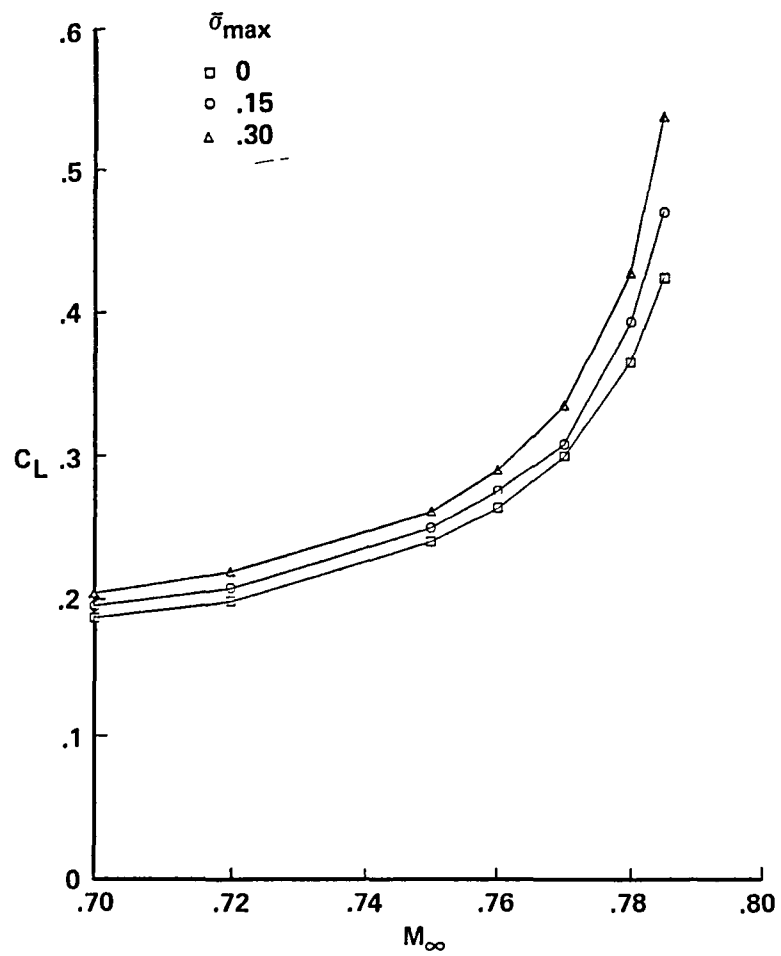


Figure 10.- Effect of varying porosity strength on the lift of a NACA 0012 airfoil at $\alpha = 1^\circ$, Type 3 porosity, $x_1 = 0.3$, $x_2 = 0.9$ (upper surface is porous).

1 Report No NASA TM-86713	2 Government Accession No	3 Recipient's Catalog No	
4 Title and Subtitle NUMERICAL STUDY OF POROUS AIRFOILS IN TRANSONIC FLOW		5 Report Date May 1985	
		6 Performing Organization Code	
7 Author(s) Chung-Lung Chen and Chen-Yen Chow (University of Colorado, Boulder, Colorado), and Terry L. Holst and William R. Van Dalsem		8 Performing Organization Report No 85209	
9 Performing Organization Name and Address NASA Ames Research Center Moffett Field, CA 94035		10 Work Unit No	
		11 Contract or Grant No	
		13 Type of Report and Period Covered Technical Memorandum	
12 Sponsoring Agency Name and Address National Aeronautics and Space Administration Washington, DC 20546		14 Sponsoring Agency Code 505-31-01	
15 Supplementary Notes Point of contact: Terry L. Holst, Ames Research Center, MS 202A-14, Moffett Field, CA 94035. (415) 694-6415 or FTS 464-6415			
16 Abstract A numerical study was made to examine the effect of a porous surface on the aerodynamic performance of a transonic airfoil. The pressure jump across the normal shock wave on the upper surface of the airfoil was reduced by making the surface below the shock porous. The weakened shock is preceded by an oblique shock at the upstream end of the porous surface where air is blown out of the cavity. The lambda shock structure shown in the numerical result qualitatively agrees with that observed in the wind tunnel. According to the present analysis, the porous airfoil has a smaller drag and a higher lift than the solid airfoil.			
17 Key Words (Suggested by Author(s)) Transonic flow Numerical methods Porous airfoils		18 Distribution Statement Unlimited Subject category: 02	
19 Security Classif (of this report) Unclassified	20 Security Classif (of this page) Unclassified	21 No of Pages 22	22 Price* A02

End of Document